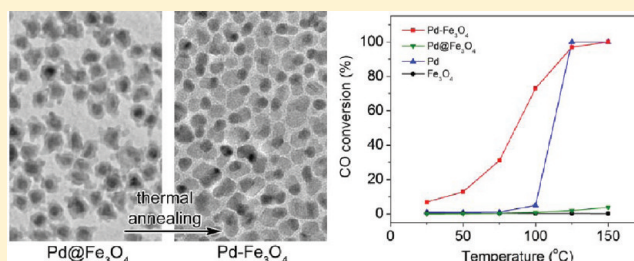


# Synthesis of Pd/Fe<sub>3</sub>O<sub>4</sub> Hybrid Nanocatalysts with Controllable Interface and Enhanced Catalytic Activities for CO Oxidation

Shutang Chen,<sup>†</sup> Rui Si,<sup>‡</sup> Eric Taylor,<sup>†</sup> Jonathan Janzen,<sup>†</sup> and Jingyi Chen<sup>\*,†</sup><sup>†</sup>Department of Chemistry and Biochemistry, University of Arkansas, Fayetteville, Arkansas 72701, United States<sup>‡</sup>Department of Chemistry, Brookhaven National Laboratory, Upton, New York 11973, United States**S** Supporting Information

**ABSTRACT:** Palladium is an important catalyst for many industrial processes and chemical reactions. The conjunction of Pd and a metal oxide is of particular interest for improving catalytic performance in heterogeneous catalysis. Here we report the synthesis of Pd/Fe<sub>3</sub>O<sub>4</sub> hybrid nanoparticles with controllable interface and the evaluation of their catalytic activities for CO oxidation. The synthesis involves a seed-mediated process in which Pd nanoparticles serve as seeds, followed by the deposition of the Fe<sub>3</sub>O<sub>4</sub> layer in the solution phase. The adhesion of the oxide layer to the metal surface is through the reduced form of Fe. Upon thermal annealing, the Fe<sub>3</sub>O<sub>4</sub> layer evolved from complete to partial coverage on the Pd core surface. This process is accompanied by increased crystallinity of Fe<sub>3</sub>O<sub>4</sub>. The resultant Pd–Fe<sub>3</sub>O<sub>4</sub> nanoparticles with a partial Fe<sub>3</sub>O<sub>4</sub> shell significantly lower the light-off temperature of CO oxidation.



Palladium plays an important role in heterogeneous catalysis for many applications including carbon–carbon coupling reactions,<sup>1–3</sup> removal of CO from the emission of automobiles,<sup>4,5</sup> conversion of chemical energy into electricity in fuel cells,<sup>6–9</sup> and energy storage.<sup>10–12</sup> Much research has focused on the morphological control of the Pd nanoparticles including size and shape.<sup>13–19</sup> It has been shown that the catalytic activity increases as the size of nanoparticles decreases due to the increase of surface area to volume ratio.<sup>20,21</sup> Additionally, the nanoparticles enclosed by high-index facets are generally more catalytically active and/or selective than those enclosed by {111} and {100} facets.<sup>22,23</sup> Nonetheless, the nanoparticles with more catalytic activity tend to be less stable and become enlarged or reshaped during reaction which compromises their activity.<sup>24,25</sup> Incorporating the metal nanoparticles with supporting materials (e.g., metal oxide) is a potentially effective route to preserve the integrity of catalysts in the reaction, thereby retaining their catalytic activities.

Metal oxides have been widely used as catalyst supports to stabilize the nanoparticles against sintering during the catalytic process.<sup>26</sup> The metal oxide could alter the electronic structure of metal nanoparticles through the interfacial bonding and/or electron transfer between the metal and the oxide.<sup>27–29</sup> More recently, studies have shown that the oxide component participates in oxidation reaction synergistically with the metal component.<sup>4,30–34</sup> While the mechanistic studies on single crystal model systems show the great promise of the hybrid system for heterogeneous catalysis, well-controlled synthesis of the catalysts is still lacking. In the past, the metal nanoparticles or a precursor to the metal were incorporated into the oxide support through impregnation, anchoring,

spreading and wetting, or deposition–precipitation.<sup>26</sup> It is hard to predict the catalytic activity and stability of the catalysts due to the lack of homogeneity in these composite materials. This has led to recent developments of the morphological controls of the metal–metal oxide hybrid nanoparticles<sup>35–38</sup> which have sought to improve the performance of the catalysts.

In this paper, a seed-mediated process has been developed to synthesize the Pd/Fe<sub>3</sub>O<sub>4</sub> hybrid nanoparticles with controllable interface between the Fe<sub>3</sub>O<sub>4</sub> shell and the Pd core. To our knowledge, this is the first observation that the interface in the hybrid nanocatalysts was controlled through nucleation and thermal annealing of nanoparticles. The Pd/Fe<sub>3</sub>O<sub>4</sub> hybrid nanoparticles were chosen because of the presence of Fe<sup>2+</sup> ion in the Fe<sub>3</sub>O<sub>4</sub> crystal structure as reducible oxide. The adhesion and contraction of Fe<sub>3</sub>O<sub>4</sub> shell at the interface was governed by the characteristics of intermediate species, reaction time, and temperature, yielding products with distinct morphologies. The catalytic activities of these hybrid nanoparticles were then evaluated for CO oxidation, a prototype reaction in many applications<sup>4</sup> such as water-gas-shift reaction, proton-exchange-membrane fuel cell, and catalytic converter. Among the nanostructures examined, the Pd–Fe<sub>3</sub>O<sub>4</sub> hybrid nanoparticles with partial Fe<sub>3</sub>O<sub>4</sub> coverage were found to significantly improve the oxidation of CO at temperatures less than 100 °C.

Received: April 15, 2012

Revised: May 12, 2012

Published: May 24, 2012



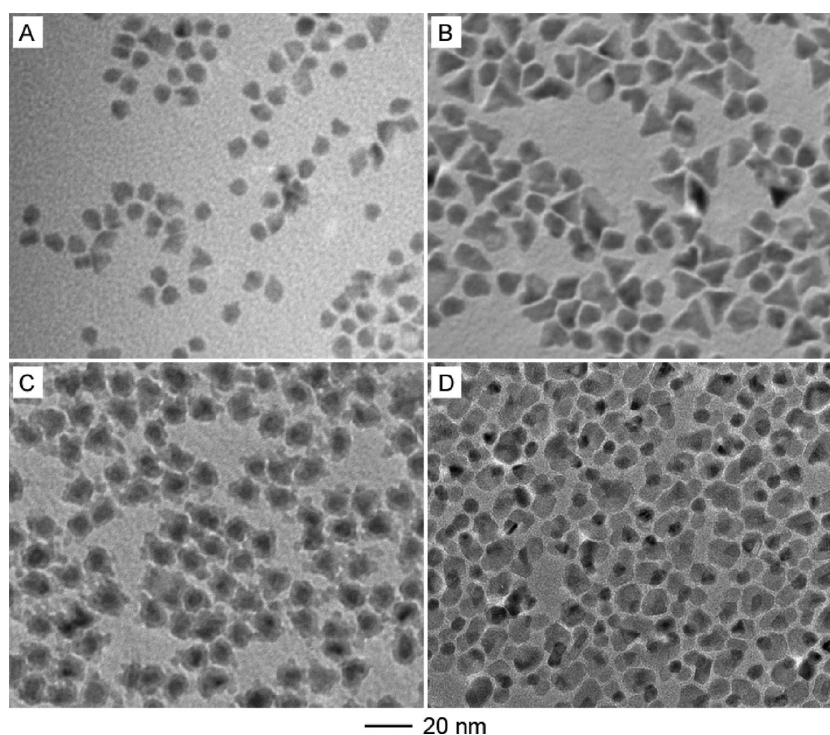


**Figure 1.** TEM images of intermediate and final products sampled at different stages of the seed-mediated process: (A) after the reaction has been heated to 160 °C, (B) after the reaction has been heated to 180 °C, (C) after the reaction has been heated to 250 °C, and (D) after the reaction has been heated to 300 °C and kept at this temperature for 30 min.

## EXPERIMENTAL SECTION

**Chemicals.** Palladium acetylacetonate ( $\text{Pd}(\text{acac})_2$ , 34.7% Pd), iron pentacarbonyl ( $\text{Fe}(\text{CO})_5$ , 99.5%), octadecene (ODE, 90%), and oleic acid (OLAC, 90%) were purchased from Alfa Aesar. Oleylamine (OLAM, 80–90%) was purchased from Aldrich. 1,2-Hexadecanediol (HDDIOL) was purchased from TCI. All chemicals were used as received.

**Synthesis of Pd/Fe<sub>3</sub>O<sub>4</sub> Hybrid Nanoparticles.** In a typical one-step synthesis,  $\text{Pd}(\text{acac})_2$  (152 mg, 0.5 mmol), HDDIOL (646 mg, 2.5 mmol), and ODE (20 mL) were added into a 100 mL three-neck flask equipped with a magnetic stir bar. The mixture was purged with argon for 30 min at room temperature and then heated to 85 °C within 1 min under argon. At 85 °C, the OLAC (190  $\mu\text{L}$ , 0.5 mmol), OLAM (175  $\mu\text{L}$ , 0.5 mmol), and  $\text{Fe}(\text{CO})_5$  (392 mg, 2.0 mmol) that had been degassed with argon bubbling were injected to the reaction mixture in order. The reaction mixture was continuously heated to 300 °C and kept at this temperature for another 30 min under argon. After that, the heating mantle was removed and the reaction was allowed to cool down to room temperature under argon. The product was precipitated out of the reaction mixture by adding 30 mL of ethanol, followed by centrifugation. The resultant black precipitate was then redispersed in toluene and collected using a combination of ethanol treatment and centrifugation. This process was repeated three times to purify the product. The final product was dispersed and stored in toluene for characterization and future use.

To study the reaction mechanism, aliquots of samples (500  $\mu\text{L}$ ) were taken out of the reaction mixture at three different temperatures (180, 250, and 300 °C) using a glass syringe and transferred to a glass vial. The product was collected and

purified as described previously. The entire purification process was performed under argon to avoid oxidation.

For the two-step process, the procedure of the first step was similar to the previous one except that the reaction was stopped immediately after the temperature heated to 250 °C. The resultant nanoparticles were purified using the same procedure as described above and redispersed in ODE for the second step. The purified nanoparticles (80 mg) were mixed with HDDIOL (258 mg, 1.0 mmol), ODE (8 mL), OLAC (74  $\mu\text{L}$ ), and OLAM (76  $\mu\text{L}$ ). The mixture was heated to 300 °C and kept at this temperature for different periods of time under argon. The products were then collected and purified using the same procedure as described above.

**Instrumentation.** Transmission electron microscopy (TEM) images were recorded using a JEOL 100cx microscope with an acceleration voltage of 100 kV. The specimens were prepared by dropping the nanoparticle dispersion onto an amorphous carbon-coated copper grid and allowing the solvent to evaporate in air. High-resolution TEM (HRTEM) images and energy-dispersive X-ray (EDX) mapping were obtained using an FEI Titan 80-300 microscope with an acceleration voltage of 300 kV.

X-ray diffraction (XRD) patterns were acquired using a Rigaku MiniFlex X-ray diffractometer equipped with  $\text{Cu K}\alpha$  radiation source operated at 30 kV/15 mA. Prior to XRD measurements, the samples were prepared by depositing nanoparticle samples on glass slides.

X-ray photoelectron spectroscopy (XPS) data were collected on an XPS spectrometer from Ulvac-phi Co. (PHI 500 Versa Probe) with  $\text{Al K}\alpha$  radiation (1486.6 eV). A powder sample was attached to carbon tape on a substrate and loaded in the XPS chamber. Calibration of the binding energy was carried out by setting the binding energy of the  $\text{C}_{1s}$  peak to 284.8 eV. The XPS spectra were fitted using Multipak software.

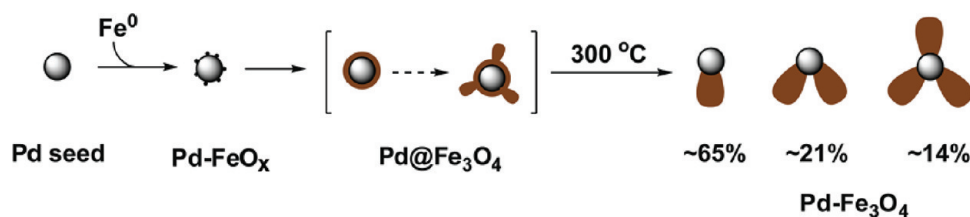


**Figure 2.** Schematic illustration of the synthesis of Pd/Fe<sub>3</sub>O<sub>4</sub> hybrid nanoparticles via the seed-mediated process.

The concentrations of Pd and Fe were determined using a GBC 932 atomic absorption (AA) spectrometer. A purified Pd–Fe<sub>3</sub>O<sub>4</sub> nanoparticle sample was dried by gently heating under argon, followed by putting it in a vacuum oven overnight. The sample was then digested with 70% HNO<sub>3</sub> and transferred into a volumetric flask to obtain a desired dilution for AA measurement. The concentrations of elemental Pd and Fe in the sample were determined from their calibration curves.

**Catalytic Activity Measurement.** The activity test for CO oxidation was conducted under a steady-state, “light-off” mode and atmospheric pressure conditions in a flow reactor equipped with a Kapton tube (o.d. = 0.125 in.). To heat the tube evenly, two small resistance heating wires were installed directly above and below the Kapton tube. The temperature was monitored with a 0.5 mm chromel/alumel thermocouple that was placed close to the sample in the Kapton tube. In a typical experiment, the fully dried nanoparticle sample, containing ~8 mg of Pd, was placed into the tube. Prior to the test, the sample was pretreated under 5% O<sub>2</sub>/95% He at 250 °C for 1 h to completely remove organic ligands (~10 wt % measured by TGA). The sample was then cooled to room temperature under 5% O<sub>2</sub>/95% He before the gas was switched to pure He. For the catalytic test, the gas stream was replaced by 1% CO/4% O<sub>2</sub>/95% He at a total flow rate of 20 mL/min. The reaction temperature was ramped from room temperature to 150 °C at 25 °C per step with 1 h duration for each step. The exit gas stream was continuously sampled and analyzed by a (0–100 amu) quadrupole mass spectrometer (QMS, Stanford Research Systems). The QMS signal intensity was monitored against the mass-to-charge ratio (*m/z*) for different gas molecules including 2(H<sub>2</sub>), 4(He), 12(C), 14(N), 16(O), 18(H<sub>2</sub>O), 28(CO or N<sub>2</sub>), 32(O<sub>2</sub>), and 44(CO<sub>2</sub>). The percentage of CO conversion (*X*<sub>CO</sub>, %) was determined by eq 1

$$X_{\text{CO}} (\%) = \left[ \frac{(\text{CO}_{\text{in}} - \text{CO}_{\text{out}})}{\text{CO}_{\text{in}}} \right] \times 100\% \quad (1)$$

where CO<sub>in</sub> and CO<sub>out</sub> represent the amount of CO<sub>in</sub> and CO<sub>out</sub>, respectively. The concentrations of CO and CO<sub>2</sub> were calibrated by certified gas tanks before each catalytic activity test.

## RESULTS AND DISCUSSION

The Pd–Fe<sub>3</sub>O<sub>4</sub> hybrid nanoparticles with controllable interface were synthesized in a one-step process. Figure 1A–D shows the TEM characterization of the products sampled from the reaction at different time periods. At the initial stage, Pd seeds were formed via thermal decomposition of Pd(acac)<sub>2</sub> in a mixture of OLAC and OLAM in the presence of HDDIOL. Upon injection of Fe(CO)<sub>5</sub> into the same reaction solution, the Fe atoms derived from the thermal decomposition of this compound evenly nucleated on the surface of each Pd nanoparticle. The Fe<sup>0</sup> incomplete shell could be partially oxidized to iron oxide (FeO<sub>*x*</sub>), probably due to the presence of a trace amount of oxidants (e.g., oxygen) in the reaction system.

Interestingly, around 50% of these nanoparticles appeared to be tetrahedra or concave tetrahedra nanocrystals with an edge length of ~10 nm, while the rest of the nanoparticles were irregular polyhedra with a size of ~6 nm. The CO released from the precursor Fe(CO)<sub>5</sub> may play a role in the synthesis. According to the single crystal study, the absorption kinetics of CO on the low-index planes [(100), (110), and (111)] are significantly different.<sup>39,40</sup> This may lead to formation of reasonably high yield of tetrahedra enclosed by {111} planes. As the reaction proceeded, Pd@Fe<sub>3</sub>O<sub>4</sub> core–shell nanoparticles were formed. Unlike the smooth core–shell structures in the previous studies,<sup>41,42</sup> these core–shell nanoparticles were composed of a Pd core of ~6 nm in diameter and a complete Fe<sub>3</sub>O<sub>4</sub> shell of ~2 nm thickness, with a few protruding Fe<sub>3</sub>O<sub>4</sub> bumps of 3–4 nm in length. To our surprise, few faceted tetrahedral cores were observed in the core–shell nanoparticles. The highly reactive corners of the tetrahedra seem to be etched by the oxidants in the system during the deposition of the Fe<sub>3</sub>O<sub>4</sub>.<sup>43,44</sup> After the reaction had proceeded for an additional 30 min at 300 °C, the Pd@Fe<sub>3</sub>O<sub>4</sub> core–shell nanoparticles evolved into a hybrid structure with a partial Fe<sub>3</sub>O<sub>4</sub> shell. Typically, the final product was a mixture of Pd–Fe<sub>3</sub>O<sub>4</sub> hybrid nanoparticles containing one (65%), two (21%), and three (14%) Fe<sub>3</sub>O<sub>4</sub> lobes on the Pd cores. The average sizes of Pd cores and Fe<sub>3</sub>O<sub>4</sub> lobes were 6.0 ± 0.8 and 7.9 ± 1.5 nm, respectively.

The evolution of the reaction process is illustrated in Figure 2. The reaction underwent three distinct stages, each of which yielded different morphologies of nanoparticles. The first stage is the adhesion of Fe<sup>0</sup> to the Pd core to yield partially covered FeO<sub>*x*</sub> thin shell to the Pd core (Pd–FeO<sub>*x*</sub>); second is the ripening and growth to generate completely covered core–shell structures (Pd@Fe<sub>3</sub>O<sub>4</sub>); third is thermal annealing to produce partially covered core–shell structures (Pd–Fe<sub>3</sub>O<sub>4</sub>). Figure 3 shows the XRD analysis of crystal structures for all three products. For the Pd–FeO<sub>*x*</sub>, the powder diffraction pattern (i.e., the positions and intensity of peaks) fitted well with that of face-centered cubic (fcc) Pd. No additional peaks were identified in the sample, suggesting that the crystalline FeO<sub>*x*</sub>, if any, would be less than ~2% of the sample. The Pd@Fe<sub>3</sub>O<sub>4</sub> and Pd–Fe<sub>3</sub>O<sub>4</sub> hybrid structures exhibited both the diffraction patterns of fcc Pd and inverse-spinel Fe<sub>3</sub>O<sub>4</sub>, suggesting that the Pd cores and the Fe<sub>3</sub>O<sub>4</sub> shells maintained their respective crystal structures during the morphological transition. The relative amounts of crystalline Fe<sub>3</sub>O<sub>4</sub> in the samples were analyzed by comparing the relative intensities of the peak corresponding to {311} planes of Fe<sub>3</sub>O<sub>4</sub> (*I*<sub>311</sub>) to the one corresponding to {111} planes of Pd (*I*<sub>111</sub>). A dramatically increased amount of crystalline Fe<sub>3</sub>O<sub>4</sub> was found in the Pd–Fe<sub>3</sub>O<sub>4</sub> hybrid structures (*I*<sub>311</sub>:*I*<sub>111</sub> = 1.1) as compared to the Pd@Fe<sub>3</sub>O<sub>4</sub> core–shell structures (*I*<sub>311</sub>:*I*<sub>111</sub> = 0.1).

The composition and structure of individual nanoparticles in the samples were further examined using EDX and HRTEM,

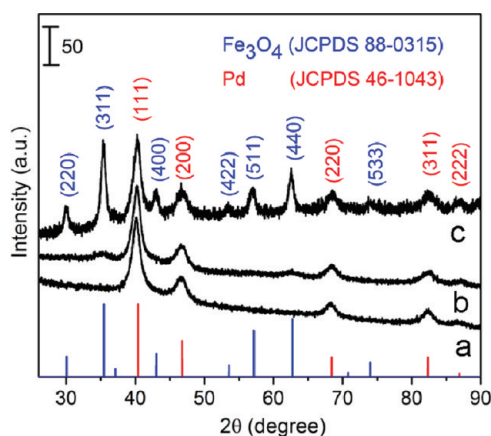


**Figure 3.** XRD patterns (a–c) corresponding to the samples shown in Figure 1B–D, respectively. The red lines and labels correspond to the face-centered-cubic crystal structure of Pd while the blue lines and labels correspond to the inverse spinel crystal structure of  $\text{Fe}_3\text{O}_4$ .

respectively. In the early stage of the reaction, no detectable elemental Fe was present in the particle (Figure 4A), possibly due to the extremely low concentration of Fe relative that of Pd (<1% atomic ratio). The HRTEM shows the lattice fringe of the representative tetrahedron in the sample was measured to be 0.223, which corresponds to the {111} planes of Pd (Figure 4E). As the reaction proceeded, the elemental Fe was evenly deposited around the Pd particle as indicated in the EDX mapping of the nanoparticle (Figure 4B). The HRTEM clearly shows a Pd@ $\text{Fe}_3\text{O}_4$  core–shell structure (Figure 4F). After

thermal annealing, the  $\text{Fe}_3\text{O}_4$  shell was contracted to localize on one side of the Pd (Figure 4C). At the same time, the  $\text{Fe}_3\text{O}_4$  recrystallized, yielding a single-crystalline structure as indicated by the continuous lattice fringe across the entire particle (Figure 4F). The presence of Fe and/or  $\text{FeO}_x$  in the early stage of the reaction remains a mystery because the XRD, EDX, and HRTEM data cannot resolve the very low Fe and/or  $\text{FeO}_x$  content in the Pd– $\text{FeO}_x$  sample.

To solve this mystery, the samples were further analyzed by XPS which has a detection limit on the order of parts per million. The oxidation state of Fe can also be distinguished based on the Fe  $2p_{3/2}$  binding energy (the energy difference between the initial and final states of the photoemission process). The Fe  $2p_{3/2}$  binding energy of  $\text{Fe}^0$  is 707.2 eV for pure Fe, whereas the binding energies of higher oxidation states are 708.2–709.4 and 710.4–711.8 eV for  $\text{Fe}^{2+}$  and  $\text{Fe}^{3+}$  species, respectively (Table S1). Both metallic Fe and oxidized species were found in the product sampled in the early stage of the reaction (Figure 5A). This result supports the previous speculation that the adhered Fe atom was partially converted to the  $\text{Fe}^{2+}$  and  $\text{Fe}^{3+}$  species in the reaction. Not surprisingly, only oxidized Fe species were found in the products (Pd@ $\text{Fe}_3\text{O}_4$  and Pd– $\text{Fe}_3\text{O}_4$ ) sampled from the later stages of the reaction (Figure 5B,C).

To investigate the structural changes in the thermal annealing process, the reaction was performed in two steps involving the first isolation of the Pd@ $\text{Fe}_3\text{O}_4$  core–shell structures and the subsequent thermal treatment. The Pd@ $\text{Fe}_3\text{O}_4$  core–shell nanoparticles were purified from the reaction mixture immediately after the reaction was heated to 250 °C.

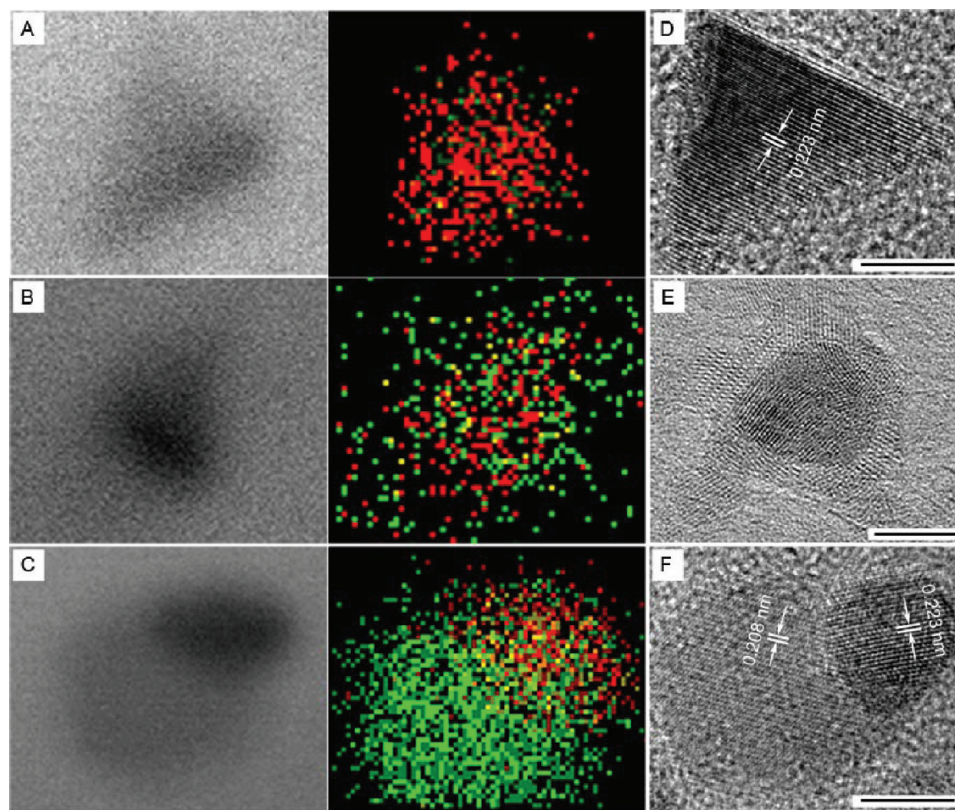


**Figure 4.** EDX elemental mapping (A–C) of representative individual nanoparticles in the samples shown in Figure 1B–D, respectively. The red represents the elemental Pd while the green represents the elemental Fe. HRTEM (D–F) of a representative individual nanoparticle in the samples shown in Figure 1B–D, respectively. The scale bar is 5 nm.

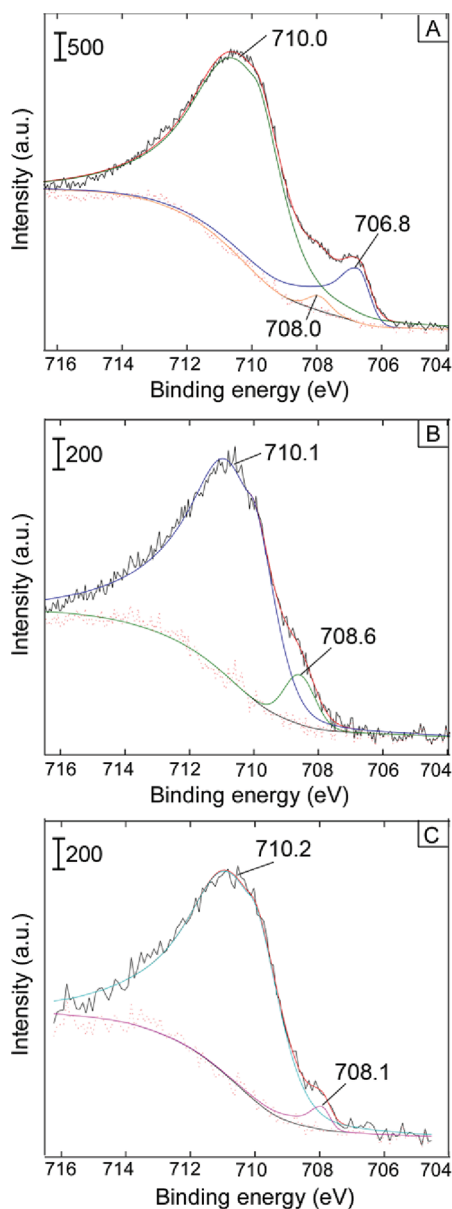


**Figure 5.** XPS spectra (A–C) of Fe  $2p_{3/2}$  (black curves) corresponding to the samples shown in Figure 1B–D, respectively. The spectra were fitted using Multipak software as indicated by the smooth color curves. The binding energy of Fe<sup>0</sup> is  $\sim 707$  eV, while the binding energy of Fe<sup>2+</sup> and Fe<sup>3+</sup> are  $\sim 708$  and  $\sim 710$  eV, respectively.

The nanoparticles were then redispersed in ODE and surfactants for thermal treatment. Figure 6 shows the TEM images of the nanoparticles that had been treated at 300 °C in solution phase for different periods of time. During this process, the nanoparticles underwent morphological changes from complete to partial Fe<sub>3</sub>O<sub>4</sub> shell on the Pd core, analogous to the contraction mechanism of a thin film deposited on a substrate.<sup>45,46</sup> Based on the comparison of the ratio of  $I_{311}$  (Fe<sub>3</sub>O<sub>4</sub>) to  $I_{111}$  (Pd), the relative amount of crystalline Fe<sub>3</sub>O<sub>4</sub> increased from 0.1, to 0.3, to 0.7 for the core–shell structures, the 30 min heat-treated sample, and the 3 h heat-treated sample, respectively. Because the amounts of the Pd and Fe<sub>3</sub>O<sub>4</sub> remain constant in these samples, the increase of the  $I_{311}$  (Fe<sub>3</sub>O<sub>4</sub>) to  $I_{111}$  (Pd) ratio suggests that the crystallinity of the Fe<sub>3</sub>O<sub>4</sub> increases with reaction time.

The electronic structure of Pd in the pure Pd and Pd–Fe<sub>3</sub>O<sub>4</sub> hybrid nanoparticles was further characterized by XPS analysis. Figure 7 shows the binding energy of Pd  $3d_{5/2}$  and  $3d_{3/2}$  for the as-prepared 6 nm Pd nanoparticles and the 6–8 nm Pd–Fe<sub>3</sub>O<sub>4</sub> hybrid nanoparticles, respectively. The binding energy of Pd 3d in the Pd–Fe<sub>3</sub>O<sub>4</sub> hybrid nanoparticles decreased by  $\sim 0.5$  eV when compared with the 6 nm Pd nanoparticles. Given that the reference peak (C<sub>1s</sub>, 284.5 eV) had no shift, the change of binding energy is likely due to the transfer of electrons from Fe<sub>3</sub>O<sub>4</sub> to Pd. In other words, the Pd in the Pd–Fe<sub>3</sub>O<sub>4</sub> hybrid nanoparticles is more electron rich (i.e., more metallic) than that in the pure Pd nanoparticles. Similar results have been observed in single crystal model catalyst study when the Pd nanoparticles were grown by vapor deposition on a thin, well-ordered Fe<sub>3</sub>O<sub>4</sub> film.<sup>47</sup> Following the heat treatment at 250 °C under 5% O<sub>2</sub>/95% He, the samples were subjected to XPS analysis again. The Pd in both samples was found to be partially oxidized as indicated by the newly arising peaks at 337.0 and 342.2 eV in the XPS spectra which correspond to Pd  $3d_{5/2}$  and  $3d_{3/2}$  of PdO, respectively (Figure 8). The Pd in the Pd–Fe<sub>3</sub>O<sub>4</sub> hybrid nanoparticles is less vulnerable to oxidation as compared to that in the pure Pd nanoparticles. It is also implied that the Pd adjacent to Fe<sub>3</sub>O<sub>4</sub> is more electron rich than the pure Pd. After heat treatment, there was no obvious change in appearance of the sample, and it remained black powder. The sample was further annealed at 500 °C under Ar for 1 h in order to determine the crystal structure of iron oxide ( $\gamma$ -Fe<sub>2</sub>O<sub>3</sub> versus Fe<sub>3</sub>O<sub>4</sub>). It is known that the  $\gamma$ -Fe<sub>2</sub>O<sub>3</sub> is unstable and changed to the stable form ( $\alpha$ -Fe<sub>2</sub>O<sub>3</sub>) at high temperature, while Fe<sub>3</sub>O<sub>4</sub> remains unchanged upon heating in Ar.<sup>48,49</sup> No  $\alpha$ -Fe<sub>2</sub>O<sub>3</sub> was found in the XRD pattern (Figure S1), suggesting that no oxidation of Fe<sub>3</sub>O<sub>4</sub> occurred after the heat treatment at 250 °C under 5% O<sub>2</sub>/95% He for 1 h.

The catalytic activities of the hybrid nanoparticles were examined for CO oxidation under the steady-state conditions. The CO conversion was plotted as a function of temperature as shown in Figure 9. The catalytic activity of pure Pd nanoparticles (Figure S2A) was measured as a benchmark for comparison. The Pd nanoparticles exhibited no CO oxidation activity at room temperature and less than 5% CO conversion at 100 °C. The CO was completely oxidized to CO<sub>2</sub> at 125 °C, at which the metal catalyst was activated, known as the ignition temperature.<sup>50,51</sup> After the conjunction with Fe<sub>3</sub>O<sub>4</sub>, the Pd@Fe<sub>3</sub>O<sub>4</sub> core–shell nanoparticles showed no catalytic activity for CO oxidation. In this case, the active sites on Pd cores were blocked completely by a few monolayers of Fe<sub>3</sub>O<sub>4</sub>. Similar reduction in the catalytic activity was found when the metal particles were covered by a thin oxide film upon heating to elevated temperature due to the strong metal–support interaction (SMSI).<sup>4</sup> Upon thermal annealing when the Pd cores were partially exposed, the Pd–Fe<sub>3</sub>O<sub>4</sub> hybrid nanoparticles drastically enhanced the rates of CO oxidation at temperatures below 100 °C. The hybrid nanoparticles began to catalyze CO oxidation with a conversion of slightly higher than 5% in 1 h at 25 °C. The CO conversion increased to 30% in 1 h at 50 °C and close to 80% in 1 h at 100 °C. Compared to the Pd/ $\alpha$ -Fe<sub>2</sub>O<sub>3</sub> nanoparticles,<sup>52</sup> the  $T_{50}$  (the temperature at which CO conversion reaches 50%) decreased by  $\sim 90$  °C. The Fe<sub>3</sub>O<sub>4</sub> nanoparticles (Figure S2B) showed no CO oxidation activity and served as a control. These results imply that the Fe<sub>3</sub>O<sub>4</sub> component in hybrid nanoparticles significantly improves Pd catalytic activity for CO oxidation at temperatures below the ignition temperature of Pd. The Fe<sub>3</sub>O<sub>4</sub> component has been

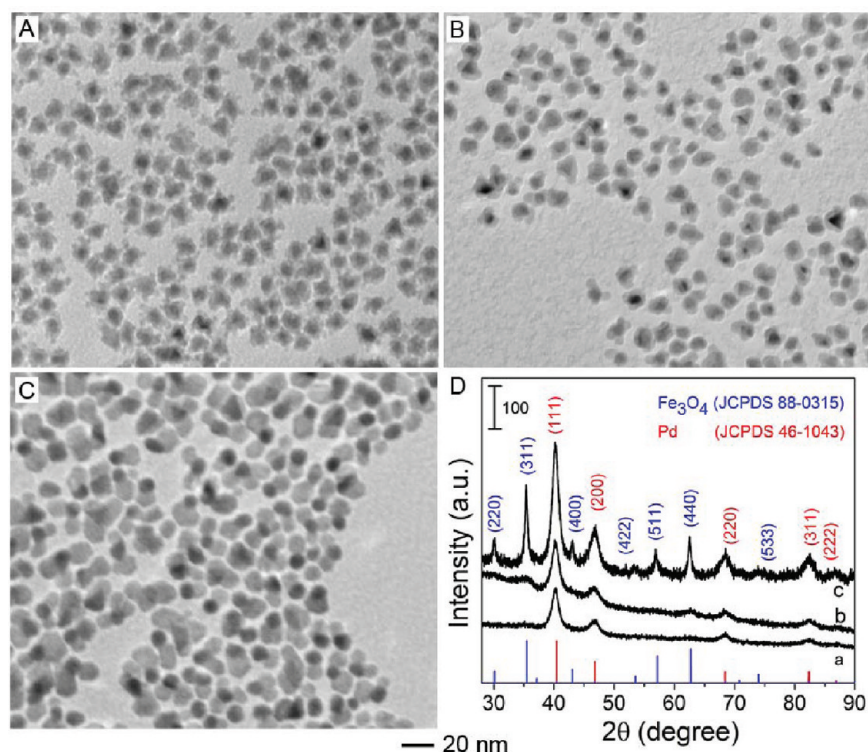


**Figure 6.** TEM images of the hybrid nanoparticles upon thermal treatment for different periods of time: (A) prior to thermal treatment, (B) treated at 300 °C for 30 min, and (C) treated at 300 °C for 3 h. (D) XRD patterns (a–c) corresponding to samples (A–C), respectively.

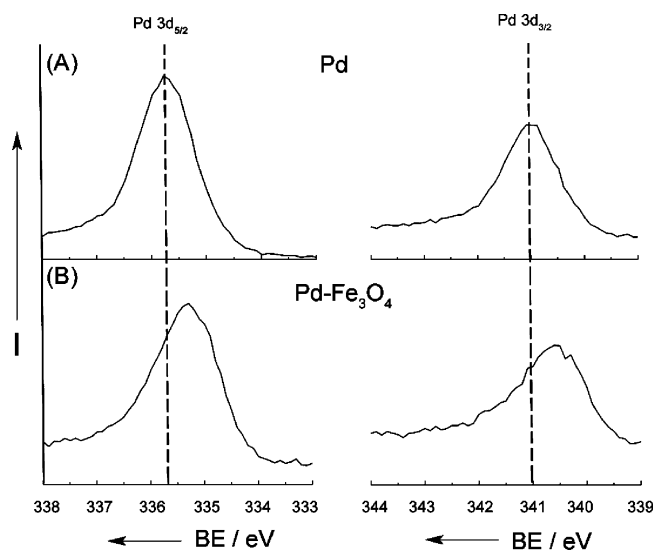


**Figure 7.** XPS spectra of Pd 3d<sub>5/2</sub> and Pd 3d<sub>3/2</sub> for the as-prepared nanoparticles: (A) Pd and (B) Pd–Fe<sub>3</sub>O<sub>4</sub>.

proposed to act as an oxygen reservoir to facilitate the oxidation reactions in the single crystal study.<sup>47,52</sup> Recent studies show that the O–Fe double layer could change to O–Fe–O trilayer by absorbing the O on the surface to activate the oxygen molecules.<sup>4,33,53–56</sup> These mechanisms might be responsible for the enhancement in catalytic activity observed for the Pd–Fe<sub>3</sub>O<sub>4</sub> hybrid nanoparticles as compared to the pure Pd nanoparticles.

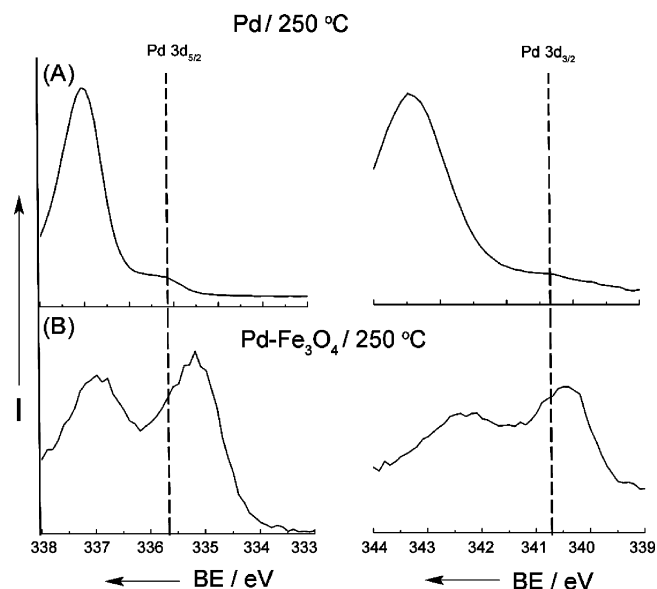


**Figure 8.** XPS spectra of Pd 3d<sub>5/2</sub> and Pd 3d<sub>3/2</sub> for the nanoparticles treated at 250 °C for 1 h under 5% O<sub>2</sub>/95% He: (A) Pd and (B) Pd–Fe<sub>3</sub>O<sub>4</sub>.

## CONCLUSION

We have successfully synthesized Pd/Fe<sub>3</sub>O<sub>4</sub> hybrid nanoparticles with controllable interface via the seed-mediated process. The adhesion of the Fe<sub>3</sub>O<sub>4</sub> component to the surface of the Pd core is through the metallic Fe. In the initial stage, the morphology of the hybrid nanoparticles was transformed from Pd–FeO<sub>x</sub> to Pd@Fe<sub>3</sub>O<sub>4</sub> nanostructures. The oxidative state of Fe evolved from zero to Fe<sup>2+</sup> and finally Fe<sup>2+</sup>/Fe<sup>3+</sup> during the progression of the reaction. In the latter stage, the Pd@Fe<sub>3</sub>O<sub>4</sub>

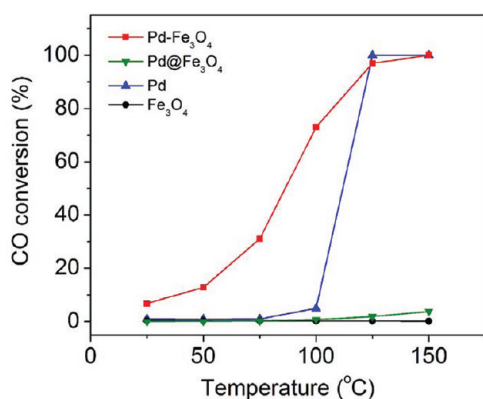


**Figure 9.** CO oxidation as a function of temperature under steady-state, light-off conditions using different types of nanoparticles: Pd-Fe<sub>3</sub>O<sub>4</sub> hybrid nanoparticles (red curve and symbols), Pd@Fe<sub>3</sub>O<sub>4</sub> core-shell nanoparticles (green curve and symbols), Pd nanoparticles (blue curve and symbols), and Fe<sub>3</sub>O<sub>4</sub> (black curve and symbols).

intermediates were ripened to yield the partially oxide covered Pd-Fe<sub>3</sub>O<sub>4</sub> hybrid nanoparticles. The seed-mediated method provides a convenient way to control the interface between the two dissimilar materials (i.e., metal and metal oxide) in the hybrid nanoparticles with well-defined morphologies. These hybrid materials could potentially become the next generation of catalysts with high activity and stability for heterogeneous catalysis.

## ASSOCIATED CONTENT

### Supporting Information

XRD characterization of the heat-treated samples; TEM and XRD characterization of the Pd and Fe<sub>3</sub>O<sub>4</sub> nanoparticles; summary of the binding energy of different oxidation states of iron. This material is available free of charge via the Internet at <http://pubs.acs.org>.

## AUTHOR INFORMATION

### Corresponding Author

\*E-mail: [chenj@uark.edu](mailto:chenj@uark.edu).

### Notes

The authors declare no competing financial interest.

## ACKNOWLEDGMENTS

This work was supported in part by the Ralph E. Powe Jr. Faculty Enhancement Award and the startup funds from the University of Arkansas (J.C.). J.J. was supported by the NSF-REU summer program at the University of Arkansas (NSF-REU0851505). The authors thank Dr. Michael Hawkrig for his help with XPS measurement and data analysis. The authors acknowledge the use of the Nano-Bio Materials Characterization Facility at the University of Arkansas.

## REFERENCES

- Molnar, A. *Chem. Rev.* **2011**, *111*, 2251–2320.
- Yin, L.; Liebscher, J. *Chem. Rev.* **2006**, *107*, 133–173.
- Miyaura, N.; Suzuki, A. *Chem. Rev.* **1995**, *95*, 2457–2483.
- Freund, H.-J.; Meijer, G.; Scheffler, M.; Schlögl, R.; Wolf, M. *Angew. Chem., Int. Ed.* **2011**, *50*, 10064–10094.
- Haag, W.; Gates, B.; Knoezinger, H. *Advances in Catalysis: The Surface Science Approach Toward Understanding Automotive Exhaust Conversion Catalysis at the Atomic Level*; Academic Press: San Diego, 1999.
- Bianchini, C.; Shen, P. K. *Chem. Rev.* **2009**, *109*, 4183–4206.
- Mazumder, V.; Sun, S. J. *Am. Chem. Soc.* **2009**, *131*, 4588–4589.
- Bai, Z.; Yang, L.; Li, L.; Lv, J.; Wang, K.; Zhang, J. *J. Phys. Chem. C* **2009**, *113*, 10568–10573.
- Zhou, W.; Lee, J. Y. *J. Phys. Chem. C* **2008**, *112*, 3789–3793.
- Yamauchi, M.; Ikeda, R.; Kitagawa, H.; Takata, M. *J. Phys. Chem. C* **2008**, *112*, 3294–3299.
- Horinouchi, S.; Yamanoi, Y.; Yonezawa, T.; Mouri, T.; Nishihara, H. *Langmuir* **2006**, *22*, 1880–1884.
- Sykes, E. C. H.; Fernández-Torres, L. C.; Nanayakkara, S. U.; Mantooth, B. A.; Nevin, R. M.; Weiss, P. S. *Proc. Natl. Acad. Sci. U. S. A.* **2005**, *102*, 17907–17911.
- Xia, Y.; Xiong, Y.; Lim, B.; Skrabalak, S. E. *Angew. Chem., Int. Ed.* **2009**, *48*, 60–103.
- Lim, B.; Jiang, M.; Tao, J.; Camargo, P. H. C.; Zhu, Y.; Xia, Y. *Adv. Funct. Mater.* **2009**, *19*, 189–200.
- Dai, Y.; Mu, X.; Tan, Y.; Lin, K.; Yang, Z.; Zheng, N.; Fu, G. J. *Am. Chem. Soc.* **2012**, *134*, 7073–7080.
- Niu, W.; Zhang, L.; Xu, G. *ACS Nano* **2010**, *4*, 1987–1996.
- Watt, J.; Young, N.; Haigh, S.; Kirkland, A.; Tilley, R. D. *Adv. Mater.* **2009**, *21*, 2288–2293.
- Huang, X.; Zheng, N. *J. Am. Chem. Soc.* **2009**, *131*, 4602–4603.
- Huang, X.; Tang, S.; Zhang, H.; Zhou, Z.; Zheng, N. *J. Am. Chem. Soc.* **2009**, *131*, 13916–13917.
- Wilson, O. M.; Knecht, M. R.; Garcia-Martinez, J. C.; Crooks, R. M. *J. Am. Chem. Soc.* **2006**, *128*, 4510–4511.
- Teranishi, T.; Miyake, M. *Chem. Mater.* **1998**, *10*, 594–600.
- Jin, M.; Zhang, H.; Xie, Z.; Xia, Y. *Angew. Chem., Int. Ed.* **2011**, *50*, 7850–7854.
- Wang, F.; Li, C.; Sun, L.-D.; Wu, H.; Ming, T.; Wang, J.; Yu, J. C.; Yan, C.-H. *J. Am. Chem. Soc.* **2010**, *133*, 1106–1111.
- Narayanan, R.; El-Sayed, M. A. *J. Phys. Chem. B* **2005**, *109*, 12663–12676.
- Narayanan, R.; El-Sayed, M. A. *J. Am. Chem. Soc.* **2003**, *125*, 8340–8347.
- Ertl, G.; Knözinger, H.; Weitkamp, J. *Handbook of Heterogeneous Catalysis*; Wiley: Weinheim, 2008; Vol. 1.
- Santra, A. K.; Goodman, D. W. *J. Phys.: Condens. Matter* **2003**, *15*, R31.
- Campbell, C. T.; Grant, A. W.; Starr, D. E.; Parker, S. C.; Bondzie, V. A. *Top. Catal.* **2000**, *14*, 43–51.
- Farmer, J. A.; Campbell, C. T. *Science* **2010**, *329*, 933–936.
- Rodriguez, J. A. *Catal. Today* **2011**, *160*, 3–10.
- Green, I. X.; Tang, W.; Neurock, M.; Yates, J. T. *Science* **2011**, *333*, 736–739.
- Widmann, D.; Behm, R. J. *Angew. Chem., Int. Ed.* **2011**, *50*, 10241–10245.
- Fu, Q.; Li, W.-X.; Yao, Y.; Liu, H.; Su, H.-Y.; Ma, D.; Gu, X.-K.; Chen, L.; Wang, Z.; Zhang, H.; Wang, B.; Bao, X. *Science* **2010**, *328*, 1141–1144.
- Rodriguez, J. A.; Ma, S.; Liu, P.; Hrbek, J.; Evans, J.; Pérez, M. *Science* **2007**, *318*, 1757–1760.
- Costi, R.; Saunders, A. E.; Banin, U. *Angew. Chem., Int. Ed.* **2010**, *49*, 4878–4897.
- Wang, C.; Xu, C.; Zeng, H.; Sun, S. *Adv. Mater.* **2009**, *21*, 3045–3052.
- Buck, M. R.; Bondi, J. F.; Schaak, R. E. *Nat. Chem.* **2012**, *4*, 37–44.
- Wang, C.; Yin, H.; Dai, S.; Sun, S. *Chem. Mater.* **2010**, *22*, 3277–3282.
- Szanyi, J.; Goodman, D. W. *J. Phys. Chem.* **1994**, *98*, 2972–2977.
- Szanyi, J.; Kuhn, W. K.; Goodman, D. W. *J. Phys. Chem.* **1994**, *98*, 2978–2981.
- Teng, X.; Black, D.; Watkins, N. J.; Gao, Y.; Yang, H. *Nano Lett.* **2003**, *3*, 261–264.
- Zeng, H.; Li, J.; Wang, Z. L.; Liu, J. P.; Sun, S. *Nano Lett.* **2004**, *4*, 187–190.
- Xiong, Y.; Wiley, B.; Chen, J.; Li, Z.-Y.; Yin, Y.; Xia, Y. *Angew. Chem., Int. Ed.* **2005**, *44*, 7913–7917.

- (44) Xiong, Y.; Chen, J.; Wiley, B.; Xia, Y.; Aloni, S.; Yin, Y. *J. Am. Chem. Soc.* **2005**, *127*, 7332–7333.
- (45) Luth, H. *Solid Surfaces, Interfaces and Thin Films*; Springer: Berlin, 2001.
- (46) Mani, S.; Saif, T. M. *Appl. Phys. Lett.* **2005**, *86*, 201903–3.
- (47) Schalow, T.; Laurin, M.; Brandt, B.; Schaueremann, S.; Guimond, S.; Kuhlenbeck, H.; Starr, D. E.; Shaikhutdinov, S. K.; Libuda, J.; Freund, H.-J. *Angew. Chem., Int. Ed.* **2005**, *44*, 7601–7605.
- (48) Sun, S.; Zeng, H.; Robinson, D. B.; Raoux, S.; Rice, P. M.; Wang, S. X.; Li, G. X. *J. Am. Chem. Soc.* **2004**, *126*, 273–279.
- (49) Yu, H.; Chen, M.; Rice, P. M.; Wang, S. X.; White, R. L.; Sun, H. *Nano Lett.* **2005**, *5*, 379–382.
- (50) Oh, S.-H.; Hoflund, G. B. *J. Phys. Chem. A* **2006**, *110*, 7609–7613.
- (51) Park, J.-N.; Forman, A. J.; Tang, W.; Cheng, J.; Hu, Y.-S.; Lin, H.; McFarland, E. W. *Small* **2008**, *4*, 1694–1697.
- (52) Jiang, X. C.; Yu, A. B. *J. Mater. Process. Technol.* **2009**, *209*, 4558–4562.
- (53) Brandt, B.; Schalow, T.; Laurin, M.; Schaueremann, S.; Libuda, J.; Freund, H. J. *J. Phys. Chem. C* **2006**, *111*, 938–949.
- (54) Sun, Y.-N.; Qin, Z. H.; Lewandowski, M.; Carrasco, E.; Sterrer, M.; Shaikhutdinov, S.; Freund, H. J. *J. Catal.* **2009**, *266*, 359–368.
- (55) Sun, Y.-N.; Giordano, L.; Goniakowski, J.; Lewandowski, M.; Qin, Z.-H.; Noguera, C.; Shaikhutdinov, S.; Pacchioni, G.; Freund, H.-J. *Angew. Chem., Int. Ed.* **2010**, *49*, 4418–4421.
- (56) Lewandowski, M.; Sun, Y.-N.; Qin, Z.-H.; Shaikhutdinov, S.; Freund, H.-J. *Appl. Catal., A* **2011**, *391*, 407–410.